JACS
JOURNAL OF THE AMERICAN CHEMICAL SOCIETY
pubs.acs.org/JACS
Article

Unveiling the Angstrom-Scale Interfacial Electron Spillover through the Metal/Electrolyte Interface

Jun Yi,[○] Yue-Jiao Zhang,[○] Yi-Fan Huang,*[,○] Jun-Rong Zheng, En-Ming You, Xiang Wang, Wei Lu, Petar M. Radjenovic, Meng Zhang, Sai Duan, Jian-Feng Li,* Bing-Wei Mao, De-Yin Wu, Bin Ren, Wolfgang Schmickler, Alexei A. Kornyshev, Xin Xu, Xiang Zhang, and Zhong-Qun Tian*

Cite This: *J. Am. Chem. Soc.* 2025, 147, 29468−29477

Read Online

ACCESS | Metrics & More | Article Recommendations | Supporting Information

ABSTRACT: The behaviors of solid−liquid interfacial electron spillovers under negative potentials are crucial for understanding heterogeneous reactions and catalysts. The missing experimental details at the angstrom scale leave the current understanding of interfacial electron spillovers largely conceptual. Herein, we demonstrated interfacial electron spillover at electrode−electrolyte interfaces by combining *in situ* electrochemical plasmon-enhanced Raman spectroscopy (PERS) with a plasmonic molecular ruler strategy. Using a series of molecules adsorbed on or proximate to metallic electrodes (Pt, Pd, Au, and Ag) as molecular rulers, the electron spillover from electrodes to electrolytes was experimentally and theoretically correlated to the PERS bands of the functional groups of rulers, which provided a spatial resolution down to the angstrom scale. The electron spillover length was highly dependent on the potentials, metals, and electrolytes. An electron spillover with a length of up to 4 Å was observed at the Ag electrode−organic electrolyte interface. These results provide quantitative measurements of the fundamental details of electronic behaviors in metal−liquid interfaces, which may guide efforts to tailor the physical and chemical properties of metals under electrochemical polarization and prospectively enable active control of quantum plasmonics for angstrom-scale interfacial sensing.

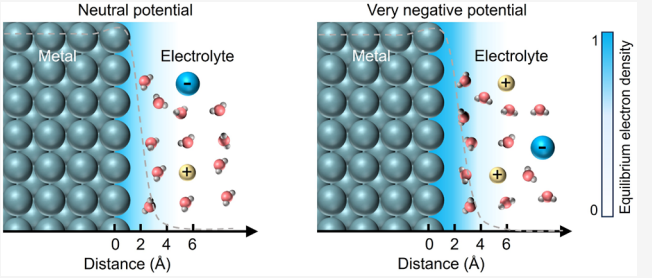

INTRODUCTION

Hydrogen evolution reaction (HER), CO_2 reduction reaction (CO_2RR), and nitrogen reduction reaction (NRR) are fundamentally important electrochemical reactions that have been considered promising solutions for sustainable development.[1,2] These electrochemical reactions are mostly triggered under significantly negative potentials with large current densities, and their properties are essentially determined by the interfacial electronic structure under such overpotentials.[1,2] One of the interesting interfacial structural evolutions under very negative potentials is the interfacial electron spillover. Due to quantum mechanical effects, electrons from metallic electrodes can spill out beyond the boundary of the metal framework for a few angstroms, a phenomenon known as interfacial electron spillover. This phenomenon critically depends on interfacial properties, such as the work function of the metal, and can be modulated by applying external potentials. Under negative potential, excessive charge usually leads to more significant electron spillover. The interfacial electron spillover could lead to nonclassical interfacial effects, such as the production of interfacial electron−hole pairs,[3] resulting in drastic changes in material properties,[4] including electric capacitance,[5] optical properties,[4] and catalytic activity.[6,7] Furthermore, electron−adsorbate interactions at the interface may also alter the chemistry of adsorbates via electron injection or promote chemical reactions by weakening chemical bond strength.[6−8] Therefore, fundamental knowledge and control of interfacial electron spillover will significantly guide interfacial chemistry and materials design, attracting tremendous attention.[4,9−13]

Since Rice's pioneering work[14] in 1928, several models have been proposed to describe interfacial electron spillover.[5,14−17] One of these models is the jellium model that correlated the features of interfacial electrons with the metal surface macroscopic properties, such as the electric double-layer capacitance, surface electro-reflectance, and the work function of metals.[5,17] Based on this model, the electrons in a metal are described as electronic jellium, while the ionic cores are represented by a constant positive background charge that abruptly drops to zero at the metal surface, forming the so-called jellium edge. The distribution of electronic jellium

Received: June 12, 2025
Revised: July 17, 2025
Accepted: July 23, 2025
Published: August 1, 2025

https://doi.org/10.1021/jacs.5c09908
J. Am. Chem. Soc. 2025, 147, 29468−29477

inherently depends on the nature of the metal electrodes and interfacial properties. Besides interfacial engineering, applying external potentials to metals is an effective way to manipulate electron spillover by modulating barriers. Although the field-induced surface atomic reconstruction process for some metals[18] (particularly single-crystal metals) may make this dependency difficult to observe, the main features of the electronic jellium tail are predicted to spill over the metal boundary and extend into the electrolyte as far as a few angstroms, depending on the applied negative potential. Unfortunately, the jellium model is predominantly limited to a few simple s-p metals used in electrochemical research, such as Hg, In, Ga, Pb, and Ag. To rationally study models with increasingly larger numbers of atoms in real chemical systems, it is highly desirable to overcome the limitations of simple s-p metals and obtain more detailed insights into electronic jellium, thereby advancing the development of a conceptually significant and efficient jellium model. Furthermore, although several techniques have been developed to study the interfacial structure at potentials close to the potential of zero charge (PZC),[19−21] it remains challenging to study interfacial electronic spillover under electrochemical potentials. This difficulty arises because experimental characterization of the electronic distribution at such an angstrom scale at metal/electrolyte interfaces is still lacking.

Here, we quantified the potential- and material-dependent angstrom-scale electron spillover at the metal/electrolyte interfaces in the potential range of hydrogen evolution by using *in situ* electrochemical plasmon-enhanced Raman spectroscopy (PERS). With the molecules adsorbed on or proximate to the metal electrodes as molecular rulers, we delved into the correlation of the electron spillover with the PERS response. The electronic spillovers on metals (Ag, Au, Pd, and Pt) and electrolytes were correlated with increased PERS intensity at negative potentials, as confirmed by theoretical modeling that couples electron spillover with surface plasmon resonance. With the molecular rulers, we explored the interfacial electronic spillover in electrochemical interfaces with respect to the electrochemical potential, electrode materials, and electrolytes. These studies provided the electron spillover length within a few angstroms not only on classic simple metals like Ag but also on Pt and Pd, which are widely used in electrochemical applications. This demonstrates the universal applicability of our method for metal electrodes, with broad relevance to both electrochemistry and materials science.

RESULTS AND DISCUSSION

Observation of Interfacial Electron Spillover from Metals into Water. Water is the most abundant compound on Earth; therefore, the interfacial electron spillover from metals to aqueous electrolytes is of great interest. Figure 1 illustrates our strategy for revealing the electron spillover at the metal/aqueous−electrolyte interface based on changes in potential-dependent PERS signals of water. The electronic density at the Ag/electrolyte interface in the absence of illumination (n_0, representing the equilibrium electron density) spills over the ionic skeleton edge of the Ag electrode and penetrates into the electrolyte, consistent with predictions from the classical jellium model.[5] To experimentally probe the spillover, PERS is utilized as a highly sensitive and powerful technique for detecting surface species.[22−24] The PERS signal of species adsorbed on or in proximity to the metal surface can

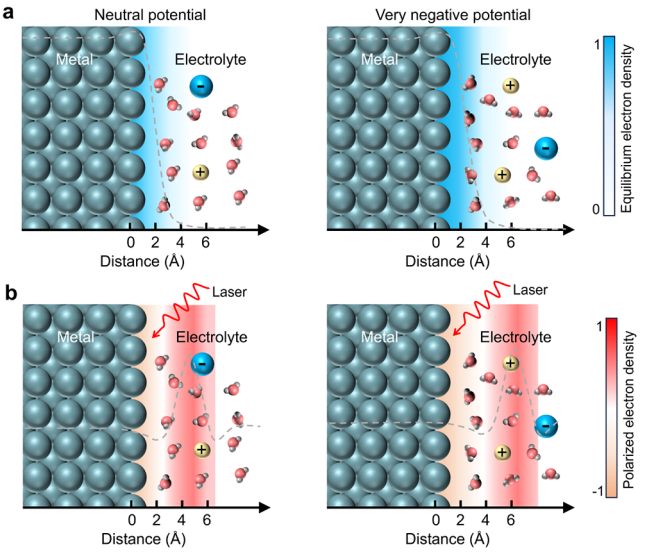

Figure 1. Schematic illustration of the interfacial electron spillover at the electrode−electrolyte interface. (**a**) Schematic illustration of the interfacial electron spillover at the electrode−electrolyte interface under neutral potentials (left panel) and very negative potentials (right panel). The cloudy blue region indicates the equilibrium electron density spillover outside the ionic skeleton edge in the absence of illumination. The gray dashed curve serves as a guideline indicating the distribution of electron density. (**b**) Schematic illustration of the polarized interfacial electron spillover under illumination. The cloudy red region indicates optically polarized electron density. The gray dashed curve serves as a guideline indicating the distribution of electron density. Molecules of different bond lengths in the red region act as molecular rulers, their potential-dependent PERS variations, which arise from the interfacial electronic response, provide a strategy to determine the spillover characteristic length.

be correlated with their distance from the surface, enabling accurate measurements at the angstrom scale in the direction perpendicular to the surface. These species act as molecular rulers, providing spatially resolved Raman spectral measurements that enable nanoscale characterization with accuracy comparable to or even higher than that of established techniques.[25−29]

The detection mechanism is based on the coupling between electron spillover and optical excitation. When the electrode is illuminated at the appropriate frequency, as in PERS experiments, the spilled electrons in the electrolyte, together with the free electron gas within the Ag framework, oscillate coherently through surface plasmon resonance. At more negative potentials, both the equilibrium electron density n_0 (Figure 1a) and the optically polarized nonequilibrium electron density n_1 (Figure 1b) upon illumination extend further from the surface, influencing different functional groups of adsorbed molecules that serve as molecular rulers. This behavior contrasts sharply with classical predictions, where both n_0 and n_1 are confined strictly to the Ag/electrolyte interface. In the quantum mechanical framework, however, ground-state electron spillover n_0 enables optically polarized electrons n_1 to extend deeply into the electrolyte, creating an extended plasmon resonance interface within the electrolyte medium. Consequently, by distinguishing PERS signal changes of molecular rulers that are directly attributable to potential-induced deformation of the surface electronic profile from

https://doi.org/10.1021/jacs.5c09908
J. Am. Chem. Soc. 2025, 147, 29468−29477

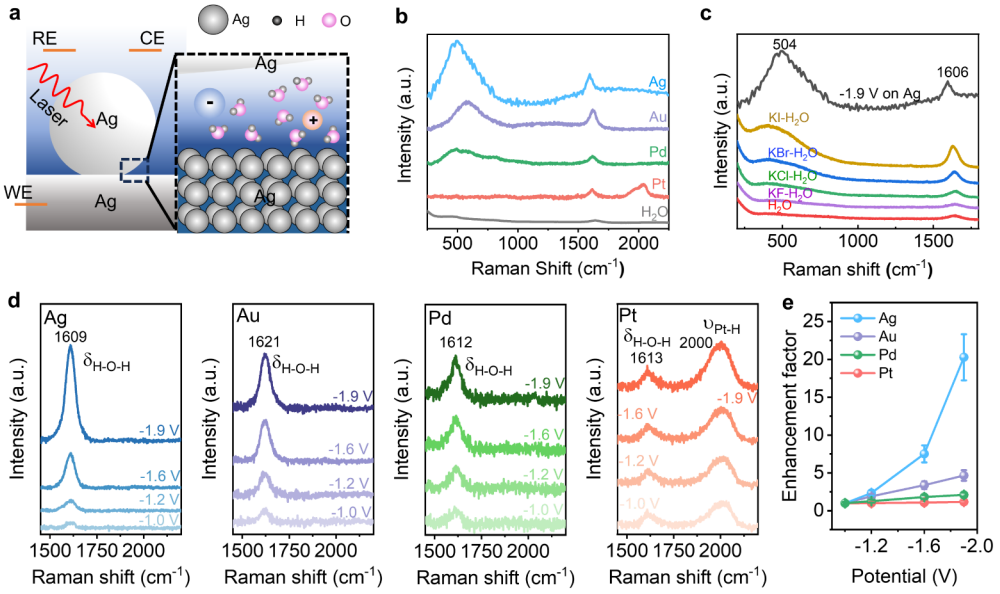

Figure 2. Correlating the changes in Raman band intensities with the interfacial electron spillover. (**a**) Schematics of the PERS experimental configuration. WE: working electrode; RE: reference electrode; CE: counter electrode. (**b**) PERS spectra of water on Ag, Au, Pd, and Pt in 0.1 M $NaClO_4$ at a potential of −1.9 V. The normal Raman spectrum of pure water is also shown for comparison. (**c**) Comparison between the PERS spectrum of water on Ag at −1.9 V in 0.1 M $NaClO_4$ and normal Raman spectra of 4 M KI, KBr, KCl, KF, and pure water. (**d**) Potential-dependent PERS spectra of water on Ag, Au, Pd, and Pt in 0.1 M $NaClO_4$. (**e**) Normalized potential-dependent PERS intensity of δ_{H-O-H} on Ag, Au, Pd, and Pt in a 0.1 M $NaClO_4$ electrolyte. Error bars indicate statistical errors from multiple measurements from five batches of samples.

other effects, we can extract quantitative information about electron spillover.

In order to comprehensively understand electron spillover on metal electrodes, Raman spectra were obtained on noble metals (Ag and Au) as well as transition metals (Pt and Pd). As shown in Figure 2a, a layer of nanoparticles was directly dispersed on and in contact with the metal electrode surfaces to induce plasmonic enhancement, mimicking the effects observed on roughened metal electrodes. For Pt and Pd electrodes, PERS enhancements were optimized using Au-core@transition-metal-shell nanoparticles (Figure S1).

As shown in Figure 2b,d, at negative potentials, the Raman spectra of water on the Ag electrode show significant alterations. A strong libration mode of water at ca. 470 cm^{-1} is observed, with an intensity even greater than that of the water bending mode (δ_{H-O-H}) at ca. 1610 cm^{-1}. Similar results were also observed from Au and Pd electrodes. This contradicts the Raman spectrum of aqueous water, where the libration mode is invisible compared with the δ_{H-O-H} mode. Notably, as shown in Figure 2b,d, the frequency of the δ_{H-O-H} mode is highly material-dependent, with 1609 cm^{-1} from the Ag electrode and 1621 cm^{-1} from the Au electrode, which is a result of the surface interaction between the metal and the O−H bonds of water. This confirms that the observed abnormal spectral features originate mainly from the interfacial water molecules that interact with the metal.

The abnormal spectral features, particularly the strong libration mode of water, are theoretically attributed to the interaction between water molecules and free electrons, where one O−H moiety from each of several water molecules is directly hydrogen-bonded to the electron, leading to dramatic changes of vibrational modes and photoabsorption characteristics of the electron-injected water.[30] This phenomenon is also evidenced by pump−probe Raman spectroscopic studies[31] (Figure S2), which demonstrate that transient electron injection into bulk solutions greatly enhances the δ_{H-O-H} and libration water modes, a phenomenon termed solvated electron-enhanced Raman scattering (EERS).[31−33] Particularly in EERS experiments with injected electrons, the broad libration mode of water becomes even more intense than the δ_{H-O-H} mode. The spectral features observed in EERS perfectly match those seen in our experiments, as shown in Figures 2a and S3, suggesting that interfacial electron spillover from the metal electrode into water occurs within this potential range in our systems. The correlation between the increase in the intensities of both δ_{H-O-H} and libration modes and electron spillover is further supported by the comparison between the PERS responses and the normal Raman spectral features of water in the solvation shell of halide anions, as shown in Figure 2b. Here, the halide anion serves as an analogue to the spilled electron that interacts with water molecules. As expected, the libration mode is strongly enhanced in this scenario. Moreover, more polarizable halide anions lead to stronger δ_{H-O-H} bands and libration modes.

However, the Raman spectra from the Pt electrode exhibit distinct features. The libration mode is kept silent, and a band of the Pt−H stretching mode (υ_{Pt-H}) with a frequency of 2000 cm^{-1} emerges. It is well-known that a full monolayer of atomic hydrogen (ca. 1.9 Å thick layer[34]) is adsorbed on the Pt surface at negative potential, where Pt−H originates from the electrochemical reduction of protons. The Pt−H layer physically isolates water from the electrode surface by a few angstroms, leading to a much weaker interaction between water and spilled electrons, as supported by the absence of the libration mode of water from the Pt electrode. We note that Pt and Pd electrodes interact differently with hydrogen: Pt forms stable surface Pt−H species that suppress electron spillover, while Pd rapidly absorbs H into the bulk lattice, enabling consistent spillover enhancement[35−37] (see Supplementary Section 11 for details).

https://doi.org/10.1021/jacs.5c09908
J. Am. Chem. Soc. 2025, 147, 29468−29477

Besides the material dependency, another interesting observation is that the intensity of the libration mode and δ_{H-O-H} also depends on the applied potential. Changes in potential from −1.0 V to −1.9 V result in a concomitant increase in the intensity of δ_{H-O-H} and the libration mode on these metal surfaces to different extents, as shown in Figure 2c. Figure 2d quantitatively summarizes the potential-dependent PERS intensities of δ_{H-O-H}, showing similar trends on Ag, Au, and Pd electrodes, with the maximum increase being up to 20 times on Ag. For the Pt electrode, due to the monolayer Pt−H adsorption, the intensity increase of the δ_{H-O-H} mode is negligible, while the υ_{Pt-H} mode increases under negative potentials. This suggests that the spilled electrons are mainly confined within the Pt−H layer, i.e., ca. 1.9 Å away from the Pt surface. Therefore, the increase in both PERS intensities of δ_{H-O-H} and υ_{Pt-H} can be used to unveil the electron spillover if a detailed correlation between them can be established.

Bridging the Electron Spillover to the Increase in PERS Enhancement of Materials at Negative Potentials. In PERS, enhancement mechanisms are typically attributed to chemical enhancement and electromagnetic (EM) enhancement. Chemical enhancement is selective for specific molecules or vibrational modes due to electronic interactions and charge transfer processes between adsorbates and the metal surface.[22] However, the universal PERS enhancement observed under negative potentials is independent of electrode material, molecules, or vibrational mode (see Supplementary Sections 1 and 4, Figure S4), indicating the predominant role of EM mechanisms. We propose that upon illumination, spillover electrons in the electrolyte become polarized and couple to the surface plasmon resonance, thereby altering the local electromagnetic field distribution at the electrode surface (Figure S5). Consequently, this modifies the Raman intensity of surface species through an enhanced electromagnetic coupling. To quantitatively correlate the measured electronic response with PERS intensities, we calculated the electromagnetic field at the surfaces of the metal electrodes under negative potentials.

We employ the quantum hydrodynamic model (QHT)[38−41] with affinity energy corrections to address the limitations of the Jellium model for common metal electrodes. The QHT has demonstrated accuracy comparable to time-dependent density functional theory (TD-DFT) while enabling a self-consistent description of interfacial electron spillover under electrochemical potentials in both equilibrium and optically polarized nonequilibrium states. The detailed QHT formulations for the electrochemical interface are described in Supplementary Sections 8−13, Figures S6-7.

The calculated electromagnetic field distribution on the Ag electrode surface (Figure 3a) reveals that with increasingly negative potential, the location of maximum electric field enhancement shifts away from the electrode surface, while the overall average field strength increases. To elucidate this behavior, we examined the electron density profile at the Ag−electrolyte interface. In the absence of illumination, the electron density remains at equilibrium, with electrons spilling over the boundary of the Ag framework and penetrating deeper into the electrolyte at more negative potentials, consistent with classical jellium model predictions.[5] Under laser illumination during PERS experiments, both the spilled electrons in the electrolyte and the free electrons in Ag collectively oscillate, generating localized surface plasmon resonance (LSPR). The optically polarized electron density n_1 exhibits similar potential-dependent spillover behaviors, as shown in Figure 3b.

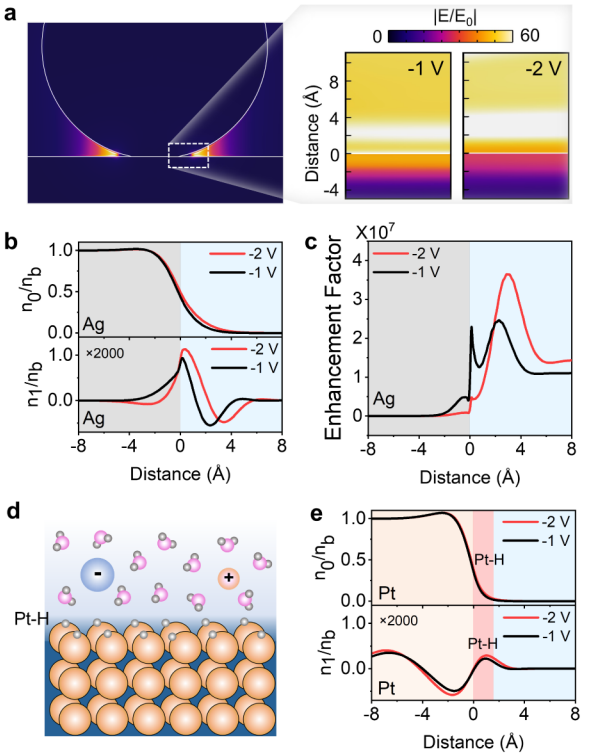

Figure 3. Electron spillover and its correlation with PERS intensity based on the QHT model. (**a**) The electromagnetic field distribution on the surface of the electrode (left panel) and a zoom-in of the hotspot regions (right panel) under −1 V and −2 V. The illumination laser is at 633 nm with a power density of 1 mW/μm^2. (**b**) The distribution of equilibrium electron density n_0 (top panel) and optically polarized nonequilibrium electron density n_1 (bottom panel, multiplied by 2000 times) across the Ag electrode−electrolyte interface. The gray shaded region indicates the Ag skeleton, and the blue shaded region indicates the electrolyte. The densities n_0 and n_1 are normalized to the ion density of the Ag skeleton n_b. (**c**) PERS enhancement factor at the interface under −1 V and −2 V. (**d**) Schematics of monolayer Pt−H adsorption on the Pt electrode surface. (**e**) The calculated n_0 and n_1 (multiplied by 2000 times) for the Pt electrode under negative potential. The red shaded region represents the Pt−H surface layer.

Unlike the classical scenario, where n_1 is confined strictly to the Ag/electrolyte interface, quantum spillover allows these polarized electrons to penetrate deeply into the electrolyte and couple with the electrode's LSPR. Since the local electromagnetic field strength is proportional to the surface density of polarized electrons, the field reaches its maximum where the density of polarized electrons in the electrolyte is greatest. More negative potentials increase the population of spilled, polarizable electrons, enhancing the field strength at the electrode surface and resulting in a consistent PERS signal increase. We therefore define the distance of maximal polarized electron density as the characteristic spillover length, as it directly relates to the experimentally observed PERS enhancement. In contrast, the common definition of spillover length, based on the center of mass of equilibrium electron density n_0, is experimentally inaccessible and unrelated to light-driven processes (Figure S9).

Based on QHT calculations, the electron spillover length at the Ag−electrolyte interface reaches 3.3 Å. The observed PERS enhancement of δ_{H-O-H} follows the order Ag > Au > Pd (Figure 2d,e), suggesting that electron spillover lengths follow

https://doi.org/10.1021/jacs.5c09908
J. Am. Chem. Soc. 2025, 147, 29468−29477

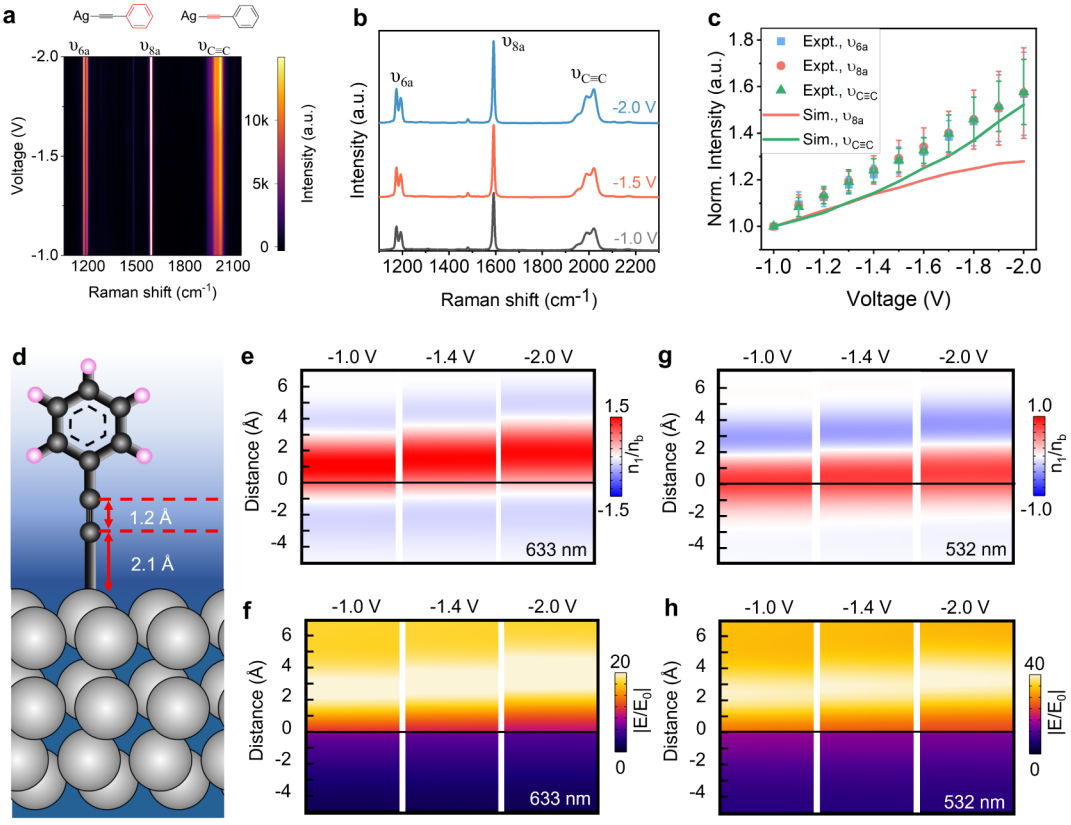

Figure 4. Measuring the length of the electron spillover on the Ag electrode in contact with the organic electrolyte. Phenylacetylene (PA) acts as a molecular ruler in tetrahydrofuran with 0.1 M tetrabutylammonium hexafluorophosphate as the organic electrolyte. (**a**) PERS spectra series of PA as a function of applied voltage under laser excitation of 633 nm. (**b**) Typical PERS spectra of PA under negative potentials. (**c**) The integrated PERS intensity of ν_{6a} (blue squares), ν_{8a} (red dots), and $\nu_{c\equiv c}$ (green triangles) modes as a function of voltage, normalized with respect to the voltage = −1.0 V case. The QHT-calculated PERS intensity of ν_{8a} (red curves) and $\nu_{c\equiv c}$ (green curves) is shown for comparison. The error bars are statistical errors obtained from multiple measurements from five batches of samples. (**d**) Schematics of the bond lengths of PA adsorbed on the Ag surface. The lengths of Ag−C and C≡C are 2.1 Å and 1.2 Å, respectively. (**e**) The calculated distribution of polarized electron spillovers n_1 under excitation of 633 nm and (**g**) 532 nm (right panel) with various applied voltages. (**f**) The calculated electric field enhancement $|E/E_0|$ under excitation of 633 nm and (**h**) 532 nm with various applied voltages. The surface of the Ag film is indicated by solid black lines (distance = 0 Å).

the same trend when using water molecules as molecular rulers. This trend is consistent with the predictions based on QHT regarding the concentration of free electrons in the bulk material and the surface charge. While surface reconstruction occurs on Au electrodes,[42,43] our polycrystalline electrodes create ensemble-averaging effects where individual grain reconstructions and surface modifications are statistically diluted across the entire electrode surface, minimizing their impact on macroscopic electron spillover behavior.

For Pt electrodes, however, hydrogen monolayer adsorption at the surface (Figure 3d) significantly alters the electrode properties and suppresses electron spillover. Our calculations show that the spillover length decreases by approximately 2 Å in the presence of the Pt−H layer (Figure S8), with spilled electrons largely confined within the ∼1.9 Å thick Pt−H region (Figure 3e). As a result, only the υ_{Pt-H} mode is enhanced at negative potentials (Figure 2d), while the δ_{H-O-H} mode of water molecules remains unchanged. This distinct behavior explains the different potential dependences of the δ_{H-O-H} intensity observed for Pt versus Pd, despite their similar bulk electronic structures.

Notably, the density of spilled electrons is only a tiny fraction of the total electron density, and therefore, the LSPR frequency remains largely unaffected with increasingly negative potential (Figure S10). The calculated PERS enhancement factor increases consistently but modestly (1.46-fold from −1 V to −2 V), matching the 1.8-fold PERS intensity change for the υ_{Pt-H} mode on the Pt electrode but significantly lower than the 20-fold enhancement observed for the δ_{H-O-H} mode on the Ag electrode (Figure S11). This quantitative discrepancy likely arises from interfacial water restructuring at highly negative potentials on the Ag electrode, as supported by molecular dynamics simulations showing water molecules reorient from a "parallel" alignment at PZC to a "two-hydrogen-down" configuration under highly negative polarization, thereby altering the Raman polarizability.[44] Interestingly, the δ_{H-O-H} intensity enhancement on the Ag electrode is much greater than that on Au or Pd electrodes (notably abrupt at −1.6 V, Figure 2d). This suggests that the electron spillover on the Ag electrode (3.3 Å based on QHT) is likely to penetrate beyond the first layer of water molecules at very negative potentials, while the electron spillover of the other metals is limited to or below the first layer, depending on the magnitude of PERS intensity increases. However, due to the elusive structure of the interfacial water molecular assemblies in the aqueous electrolyte and since the first layer of water molecules can be attached differently to these electrodes, it is difficult to precisely quantify the electron spillover length based on the PERS of water.

https://doi.org/10.1021/jacs.5c09908
J. Am. Chem. Soc. 2025, 147, 29468−29477

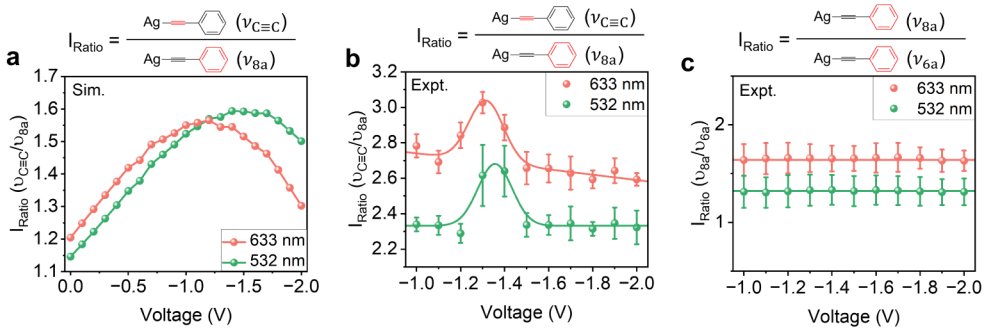

Figure 5. Quantitative measurement of electron spillovers. (**a**) The QHT-calculated PERS intensity ratio between $\nu_{c\equiv c}$ and ν_{8a} modes. (**b**) The measured PERS intensity ratio between $\nu_{c\equiv c}$ and ν_{8a} mode. (**c**) The measured PERS intensity ratio between ν_{8a} and ν_{6a}. Two cases with excitation wavelengths of 633 nm (red dots) and 532 nm (green dots) are shown. The error bars represent statistical errors obtained from multiple measurements.

Quantitative Measurement of Electron Spillover Length. To quantitatively determine the electron spillover length at the angstrom scale, we refined the molecular ruler approach by employing organic molecules with two functional groups. Ideal rulers would be those that are chemically attached to the metal surface and remain chemically stable under applied potentials. However, a densely packed monolayer of such molecules may substantially alter the interfacial properties and electron spillover dynamics, as demonstrated in the Pt−H monolayer case. In that scenario, the measured characteristics reflect the modified, rather than the bare, electrode−electrolyte interface. Therefore, submonolayer coverage is preferable in this respect.

In this context, phenylacetylene (PA) was chemically anchored to the Ag electrode via dehydrogenative adsorption, offering both stability and a well-defined orientation. The PERS spectra of submonolayer PA display three major Raman bands: the ν_{6a} (1185 cm^{-1}) and ν_{8a} (1592 cm^{-1}) modes associated with benzene ring breathing and the $\nu_{c\equiv c}$ (2000 cm^{-1}) mode assigned to the acetylenic C≡C stretch. Apart from intensity changes, the spectral features—positions and relative patterns—remain unaffected by increasingly negative potentials (Figure 4b), confirming the chemical and geometric stabilities of the PA layer during electrochemical modulation.

Remarkably, all three PA bands exhibit synchronous intensity enhancement with negative potential, with the average PERS intensity increasing by a factor of 1.5 from −1 V to −2 V, in excellent quantitative agreement with QHT simulations. Density functional theory (DFT) calculations show that PA adsorbs nearly vertically on Ag with Ag−C, C≡C, and C-phenyl bond lengths of 2.1, 1.2, and 1.4 Å, respectively (Figure 4d). QHT results indicate that upon increasingly negative potential, the spatial distribution of optically polarized spillover electrons advances progressively from the vicinity of the Ag−C bond toward the C≡C bond region (Figure 4e). This angstrom-scale modulation, dictated by the applied potential, allows for quantitative determination of the spillover length using the characteristic bond distances of PA as an internal reference. Crucially, the local electromagnetic field experienced by the C≡C bond site, which effectively acts as a probe along the molecular axis, shows a more pronounced potential dependency than that of the distant phenyl group (Figure 4f).

Owing to the rigid structure of the PA molecule and the parallel orientation of the dipoles of the $\nu_{c\equiv c}$ and ν_{8a} modes, the relative enhancement of the two modes serves as a sensitive and spatially resolved indicator of field gradients along the molecular rod. Specifically, the intensity ratio of $\nu_{c\equiv c}$ versus ν_{8a} goes through a maximum with negatively changing potential, peaking at roughly −1.3 V before returning to the baseline (Figure 5a,b). Notably, the relative intensity between ν_{8a} and ν_{6a} remains constant (Figure 5c), corroborating that the observed change is not due to general surface effects or molecular reorientation but rather to the spatial progression of field enhancement driven by electron spillover. Changing the excitation wavelength to 532 nm yields the same trend (Figure S12), but with the peak position shifted negatively by 0.1 V, consistent with EM field redistribution rather than photochemical changes. This wavelength-dependent shift is rationalized by QHT calculations, which attribute it to the dielectric dispersion and the LSPR properties of the Ag electrode: under 532 nm excitation, the region of polarized electron spillover is located closer to the metallic surface, so a more negative potential is necessary for the spillover to reach the C≡C region.

While quantitative differences exist between theoretical and experimental voltage ranges and curve shapes, the QHT calculations demonstrate consistent trends for both wavelength-dependent electron distribution and potential-dependent intensity ratios, showing good qualitative agreement with experimental findings despite narrower experimental peaks suggesting more localized electric field distributions.[45] From this combined experimental and theoretical analysis, we robustly determined the characteristic length of electron spillover under illumination at −2.0 V to be approximately 3.5 Å from the Ag surface. This value provides a quantitative benchmark linking the electromagnetic field distribution at the electrochemical interface to the measured molecular-scale spectroscopic response.

■ CONCLUSIONS

We probed the electronic behaviors of metal electrodes under significant negative potentials by using the *in situ* PERS technique. This approach revealed a new interfacial structure with electron spillover under significant overpotentials and its interactions with surface species. The spilled electrons extend into the electrolyte and selectively polarize specific chemical bonds of interfacial species, which act as molecular/atomic rulers to quantitatively capture the electron spillover length. These results lend quantitative support to a long-term concept of electron spillover from metal electrodes and can be extended to more general interfacial systems, such as electron−hole pair

https://doi.org/10.1021/jacs.5c09908
J. Am. Chem. Soc. 2025, 147, 29468−29477

generation across metal/semiconductor interfaces. They provide experimental evidence of the quantum nature of the electronic response at these interfaces upon applied potentials, which was previously speculated to be important in electrochemical kinetics and tunneling spectroscopy.[46] These findings may improve the understanding of interfacial physics and chemistry in energy conversion and electrocatalysis fields, such as water electrolysis.

METHODS

The Preparation of PERS-Active Ag, Au, Pd, and Pt Electrodes. The silver electrode was polished with alumina powder with sizes of 1 and 0.3 μm in sequence. The sol of the Ag particles with a mean size of ca. 80 nm was prepared by reducing 200 mL of boiling $AgNO_3$ solution with a concentration of 1 mmol/L by adding 6 mL of 1 wt % sodium citrate solution. After three centrifugation cycles, the sol was dropped onto the polished silver electrode and dried in a vacuum desiccator.

The gold electrode was polished with alumina powder with sizes of 1 and 0.3 μm in sequence. After being polished and sonicated, the gold electrode was transferred into an electrochemical cell. In 0.5 mol/L H_2SO_4 solution, cyclic voltammetry ranging from −0.25 to 1.4 V (vs SCE) was performed on the gold electrode in order to remove the surface-active sites formed during the polishing process. The sol of the Au particles with a mean size of ca. 55 nm was prepared by reducing 200 mL of boiling $HAuCl_4$ solution with a concentration of 0.01 wt % by adding 1.4 mL of 1 wt % sodium citrate solution while boiling.[47] After three centrifugation cycles, the sol was dropped onto the polished gold electrode and dried in a vacuum desiccator.

The palladium electrode was polished with alumina powder with sizes of 1 and 0.3 μm in sequence. After polishing and sonication, the palladium electrode was transferred into the electrochemical cell. In a 0.5 mol/L H_2SO_4 solution, cyclic voltammetry ranging from −0.2 to 1.25 V (vs SCE) was performed on the palladium electrode to remove the surface-active sites formed during the polishing process. The 55 nm Au-core @ 1.4 nm Pd-shell particles were synthesized for the preparation of the PERS-active Pd electrode.[48,49] First, the sol of Au particles with a size of 55 nm was synthesized by using the procedure described above. Then, 17.5 mL of water and 1.64 mL of 1 mmol/L H_2PdCl_4 were added to 30 mL of Au sol under vigorous stirring at 4 °C. Subsequently, 0.82 mL of 10 mmol/L ascorbic acid solution was slowly added to the system. Finally, the 55 nm Au-core @ 1.4 nm Pd-shell particles were prepared by maintaining the temperature for 30 min. After three centrifugation cycles, the sol was dropped onto the polished palladium electrode and dried in a vacuum desiccator.

The platinum electrode was polished with alumina powder with sizes of 1 and 0.3 μm in sequence. After polishing and sonication, the platinum electrode was transferred into the electrochemical cell. In a 0.5 mol/L H_2SO_4 solution, cyclic voltammetry ranging from −0.3 to 1.25 V (vs SCE) was performed on the platinum electrode in order to remove the surface active sites formed during the polishing process. The 55 nm Au-core @ 1.4 nm Pt-shell particles were synthesized for the preparation of the PERS-active Pt electrode.[48,50] First, the sol of Au particles with a size of 55 nm was synthesized using the procedure described above. Then, 17.8 mL of water and 1.47 mL of 1 mmol/L H_2PtCl_6 solution were added to 30 mL of Au sol under vigorous stirring at 80 °C. Subsequently, 0.74 mL of 10 mmol/L ascorbic acid solution was slowly added to the system. Finally, the 55 nm Au-core @ 1.4 nm Pt-shell particles were prepared by maintaining the reaction temperature for 30 min. After three centrifugation cycles, the sol was dropped onto the polished platinum electrode and dried in a vacuum desiccator.

The reagents $AgNO_3$, $HAuCl_4$, H_2PdCl_4, and H_2PtCl_4 were purchased from Sinopharm Chemical Reagent Co., Ltd. Highly pure KCl, KBr, KI, and $NaClO_4$ were purchased from Alfa Aesar. Phenyl isocyanide was purchased from Hangzhou Yi Lu Biological Technology Co., Ltd., and it was characterized by ^{1}H NMR (Bruker Advance II 400 MHz calibrated with tetramethylsilane. Solvent: $CDCl_3$, ^{1}H NMR (ppm): δ = 7.40 (m)). The ultrapure water with an electrical resistivity of 18.2 MΩ·cm used in all experiments was obtained from a Milli-Q system.

***In Situ* EC-PERS Measurement.** The prepared PERS-active electrodes were transferred to a custom-made spectroelectrochemical cell with a three-electrode configuration. A saturated calomel electrode (SCE) and a platinum wire were used as the reference and counter electrodes, respectively. The Raman spectroscopic measurements were performed using Dilor and XploRA (Jobin Yvon-Horiba, France) confocal Raman microscopes. The two systems feature lasers with wavelengths of 532 nm (XploRA) and 632.8 nm (Dilor). The electrochemical potential was applied using the electrochemical potentiostat CHI 631B, manufactured by Shanghai Chenhua Instruments Limited (SCHI).

Quantum Hydrodynamic Theory Calculation. In QHT, the electron gas is then fully described by macroscopic hydrodynamic quantities. We used an energy functional $G[n(r,t)]$ to describe the kinetic energy, exchange energy, and correlation energy of the interacting electrons.[40] The electron density distribution of equilibrium static states (taken as the ground-state density, n_0) was obtained. A Neumann boundary condition[41] was used to obtain the potential-dependent n_0. The electron density distribution under optical illumination (taken as the polarized electron density, n_1) was obtained by coupling the hydrodynamic equations to Maxwell's equations and linearizing the system using the perturbation approach. The equations were solved using a commercial finite-element method software package, COMSOL Multiphysics. The details of QHT formulations, numerical implementation, calibration of QHT, characteristic length of electron spillover, and discussions on interfacial water and Pt−H adsorption are elaborated in the supplementary sections.

Density Functional Theory (DFT) Calculation. The geometric optimizations of Pt−H and Ag−PA systems were performed on a slab model using DFT with the Vienna Ab Initio Simulation Package.[51] The projector augmented wave method (PAW)[52] and the Perdew−Burke−Ernzerhof generalized-gradient approximation (GGA-PBE) functional[53] were applied. The Pt(111)-$\sqrt{3}\times\sqrt{3}$ and Ag(111)-3 × 3 slabs were employed to describe Pt and Ag surfaces, with Monkhorst−Pack k-point sampling of 9 × 9 × 1, respectively. An energy cutoff of 450 eV and a first-order Methfessel−Paxton smearing with a sigma of 0.2 were applied.[54] The thickness of the vacuum layer was set to 30 Å. The lattice constants of 3.9864 Å and 4.164 Å were used for Pt and Ag, respectively.[55,56] Two layers at the bottom were fixed, while three layers were fully relaxed for the simulation of the surface.

https://doi.org/10.1021/jacs.5c09908
J. Am. Chem. Soc. 2025, 147, 29468−29477

■ ASSOCIATED CONTENT

Data Availability Statement

The data that support the findings of this study are available from the corresponding author upon reasonable request.

Supporting Information

The Supporting Information is available free of charge at https://pubs.acs.org/doi/10.1021/jacs.5c09908.

General considerations in terms of the PERS mechanisms; *in situ* EC-PERS measurement; electron-enhanced Raman scattering of water: from time-resolved electron-enhanced Raman scattering to static (surface-enhanced) Raman scattering; electrolyte-dependent electron spillover; potential-dependent surface charge; comparison between conventional PERS and the gain of the electron spillover-PERS intensity at the negative potential; density functional theory calculation; basic formulations of the quantum hydrodynamic model; calibration of the QHT model via the metal-vacuum work function; voltage-dependent ground-state electron spillover at the electrode−electrolyte interfaces; monolayer Pt−H adsorption at the Pt electrode; determination of the characteristic length of electron spillover; optical response of Ag electrodes with electron spillover; the potential-dependent υ_{Pt-H} intensity; potential-dependent PERS of PA under 532 nm excitation; potential-dependent C−C triple bond frequency shifts; surface relaxation and reconstruction effects; Figure S1−Figure S15 and Table S1 (PDF)

■ AUTHOR INFORMATION

Corresponding Authors

Zhong-Qun Tian − *School of Electronic Science and Engineering, The State Key Laboratory of Physical Chemistry of Solid Surfaces, College of Chemistry & Chemical Engineering, College of Energy, Fujian Key Laboratory of Ultrafast Laser Technology and Applications, Xiamen University, Xiamen 361005, P. R. China;* orcid.org/0000-0002-9775-8189; Email: zqtian@xmu.edu.cn

Jian-Feng Li − *School of Electronic Science and Engineering, The State Key Laboratory of Physical Chemistry of Solid Surfaces, College of Chemistry & Chemical Engineering, College of Energy, Fujian Key Laboratory of Ultrafast Laser Technology and Applications, Xiamen University, Xiamen 361005, P. R. China;* orcid.org/0000-0003-1598-6856; Email: li@xmu.edu.cn

Yi-Fan Huang − *School of Physical Science and Technology, ShanghaiTech University, Shanghai 201210, P. R. China;* orcid.org/0000-0002-0615-0814; Email: huangyf@shanghaitech.edu.cn

Authors

Jun Yi − *School of Electronic Science and Engineering, The State Key Laboratory of Physical Chemistry of Solid Surfaces, College of Chemistry & Chemical Engineering, College of Energy, Fujian Key Laboratory of Ultrafast Laser Technology and Applications, Xiamen University, Xiamen 361005, P. R. China; Nanoscale Science and Engineering Center, University of California, Berkeley, California 94720, United States;* orcid.org/0000-0003-2186-6615

Yue-Jiao Zhang − *School of Electronic Science and Engineering, The State Key Laboratory of Physical Chemistry of Solid Surfaces, College of Chemistry & Chemical Engineering, College of Energy, Fujian Key Laboratory of Ultrafast Laser Technology and Applications, Xiamen University, Xiamen 361005, P. R. China;* orcid.org/0000-0002-7264-277X

Jun-Rong Zheng − *School of Electronic Science and Engineering, The State Key Laboratory of Physical Chemistry of Solid Surfaces, College of Chemistry & Chemical Engineering, College of Energy, Fujian Key Laboratory of Ultrafast Laser Technology and Applications, Xiamen University, Xiamen 361005, P. R. China*

En-Ming You − *School of Electronic Science and Engineering, The State Key Laboratory of Physical Chemistry of Solid Surfaces, College of Chemistry & Chemical Engineering, College of Energy, Fujian Key Laboratory of Ultrafast Laser Technology and Applications, Xiamen University, Xiamen 361005, P. R. China;* orcid.org/0000-0001-6310-5908

Xiang Wang − *School of Electronic Science and Engineering, The State Key Laboratory of Physical Chemistry of Solid Surfaces, College of Chemistry & Chemical Engineering, College of Energy, Fujian Key Laboratory of Ultrafast Laser Technology and Applications, Xiamen University, Xiamen 361005, P. R. China;* orcid.org/0000-0003-1937-0725

Wei Lu − *School of Electronic Science and Engineering, The State Key Laboratory of Physical Chemistry of Solid Surfaces, College of Chemistry & Chemical Engineering, College of Energy, Fujian Key Laboratory of Ultrafast Laser Technology and Applications, Xiamen University, Xiamen 361005, P. R. China*

Petar M. Radjenovic − *School of Electronic Science and Engineering, The State Key Laboratory of Physical Chemistry of Solid Surfaces, College of Chemistry & Chemical Engineering, College of Energy, Fujian Key Laboratory of Ultrafast Laser Technology and Applications, Xiamen University, Xiamen 361005, P. R. China*

Meng Zhang − *School of Electronic Science and Engineering, The State Key Laboratory of Physical Chemistry of Solid Surfaces, College of Chemistry & Chemical Engineering, College of Energy, Fujian Key Laboratory of Ultrafast Laser Technology and Applications, Xiamen University, Xiamen 361005, P. R. China*

Sai Duan − *MOE Key Laboratory of Computational Physical Sciences, Department of Chemistry, Fudan University, Shanghai 200433, P. R. China;* orcid.org/0000-0002-3282-0711

Bing-Wei Mao − *School of Electronic Science and Engineering, The State Key Laboratory of Physical Chemistry of Solid Surfaces, College of Chemistry & Chemical Engineering, College of Energy, Fujian Key Laboratory of Ultrafast Laser Technology and Applications, Xiamen University, Xiamen 361005, P. R. China;* orcid.org/0000-0002-9015-0162

De-Yin Wu − *School of Electronic Science and Engineering, The State Key Laboratory of Physical Chemistry of Solid Surfaces, College of Chemistry & Chemical Engineering, College of Energy, Fujian Key Laboratory of Ultrafast Laser Technology and Applications, Xiamen University, Xiamen 361005, P. R. China;* orcid.org/0000-0001-5260-2861

Bin Ren − *School of Electronic Science and Engineering, The State Key Laboratory of Physical Chemistry of Solid Surfaces, College of Chemistry & Chemical Engineering, College of Energy, Fujian Key Laboratory of Ultrafast Laser Technology and Applications, Xiamen University, Xiamen 361005, P. R. China;* orcid.org/0000-0002-9821-5864

Wolfgang Schmickler − *Institute of Theoretical Chemistry, Ulm University, Ulm D-89069, Germany;* orcid.org/0000-0003-4162-6010

Alexei A. Kornyshev − *Department of Chemistry, Molecular Sciences Research Hub, Imperial College London, White City Campus, London W12 0BZ, U.K.;* orcid.org/0000-0002-3157-8791

Xin Xu − *MOE Key Laboratory of Computational Physical Sciences, Department of Chemistry, Fudan University, Shanghai 200433, P. R. China;* orcid.org/0000-0002-5247-2937

Xiang Zhang − *Nanoscale Science and Engineering Center, University of California, Berkeley, California 94720, United States; Faculty of Science and Faculty of Engineering, The University of Hong Kong, Hong Kong 999077, P. R. China*

Complete contact information is available at: https://pubs.acs.org/10.1021/jacs.5c09908

Author Contributions

○J.Y., Y.-J.Z., and Y.-F.H. contributed equally to this work

Notes

The authors declare no competing financial interest.

■ ACKNOWLEDGMENTS

This work is financially supported by the National Natural Science Foundation of China (22272140, 21872094, 21991152, 22474116 and 21991150), the National Key Research and Development Program of China (2024YFA1210803), the ShanghaiTech University Starting-Up Grant, and the Fundamental Research Funds for the Central Universities (20720240068). The HPC Platform of ShanghaiTech University Library and Information Services is acknowledged for the use of their supercomputer facilities.

■ REFERENCES

(1) Chen, S.; Takata, T.; Domen, K. Particulate photocatalysts for overall water splitting. *Nat. Rev. Mater.* **2017**, *2* (10), 17050.

(2) Suryanto, B. H. R.; Du, H.-L.; Wang, D.; Chen, J.; Simonov, A. N.; MacFarlane, D. R. Challenges and prospects in the catalysis of electroreduction of nitrogen to ammonia. *Nat. Catal.* **2019**, *2* (4), 290−296.

(3) Jin, D.; Hu, Q.; Neuhauser, D.; von Cube, F.; Yang, Y.; Sachan, R.; Luk, T. S.; Bell, D. C.; Fang, N. X. Quantum-Spillover-Enhanced Surface-Plasmonic Absorption at the Interface of Silver and High-Index Dielectrics. *Phys. Rev. Lett.* **2015**, *115* (19), 193901.

(4) Yang, Y.; Zhu, D.; Yan, W.; Agarwal, A.; Zheng, M.; Joannopoulos, J. D.; Lalanne, P.; Christensen, T.; Berggren, K. K.; Soljačić, M. A general theoretical and experimental framework for nanoscale electromagnetism. *Nature* **2019**, *576* (7786), 248−252.

(5) Schmickler, W. Electronic Effects in the Electric Double Layer. *Chem. Rev.* **1996**, *96* (8), 3177−3200.

(6) Stefancu, A.; Halas, N. J.; Nordlander, P.; Cortes, E. Electronic excitations at the plasmon−molecule interface. *Nat. Phys.* **2024**, *20* (7), 1065−1077.

(7) Stewart, S.; Wei, Q.; Sun, Y. Surface chemistry of quantum-sized metal nanoparticles under light illumination. *Chem. Sci.* **2021**, *12* (4), 1227−1239.

(8) Mason, P. E.; Schewe, H. C.; Buttersack, T.; Kostal, V.; Vitek, M.; McMullen, R. S.; Ali, H.; Trinter, F.; Lee, C.; Neumark, D. M.; Thürmer, S.; Seidel, R.; Winter, B.; Bradforth, S. E.; Jungwirth, P. Spectroscopic evidence for a gold-coloured metallic water solution. *Nature* **2021**, *595* (7869), 673−676.

(9) Kittel, C.; McEuen, P. *Introduction to solid state physics*; John Wiley & Sons: New Jersey, USA, 2018.

(10) Somorjai, G. A.; Li, Y. *Introduction to Surface Chemistry and Catalysis*, Second ed.; John Wiley & Sons: Hoboken, New Jersey, U.S.A, 2010; p. 800.

(11) Norskov, J. K.; Bligaard, T.; Rossmeisl, J.; Christensen, C. H. Towards the computational design of solid catalysts. *Nat. Chem.* **2009**, *1* (1), 37−46.

(12) Kornyshev, A. A.; Spohr, E.; Vorotyntsev, M. A.Electrochemical Interfaces: At the Border Line*Encyclopedia of Electrochemistry*Wiley200733−132

(13) Wang, Z.; Chen, M.; Wu, J.; Ji, X.; Zeng, L.; Peng, J.; Yan, J.; Kornyshev, A. A.; Mao, B.; Feng, G. Constant-Potential Modeling of Electrical Double Layers Accounting for Electron Spillover. *Phys. Rev. Lett.* **2025**, *134* (4), 046201.

(14) Rice, O. K. Application of the Fermi Statistics to the Distribution of Electrons Under Fields in Metals and the Theory of Electrocapillarity. *Phys. Rev.* **1928**, *31* (6), 1051.

(15) Goodisman, J. Electrochemical potentials for charged metal spheres in the Thomas−Fermi−Dirac jellium model. *J. Chem. Phys.* **1975**, *63* (10), 4437−4441.

(16) Kornyshev, A. A.; Schmickler, W.; Vorotyntsev, M. A. Nonlocal electrostatic approach to the problem of a double layer at a metal-electrolyte interface. *Phys. Rev. B* **1982**, *25* (8), 5244.

(17) Kornyshev, A. A. Metal electrons in the double layer theory. *Electrochim. Acta* **1989**, *34* (12), 1829−1847.

(18) Kornyshev, A. A.; Vilfan, I. Phase transitions at the electrochemical interface. *Electrochim. Acta* **1995**, *40* (1), 109−127.

(19) Yamakata, A.; Osawa, M. Destruction of the Hydration Shell around Tetraalkylammonium Ions at the Electrochemical Interface. *J. Am. Chem. Soc.* **2009**, *131* (20), 6892−6893.

(20) Montenegro, A.; Dutta, C.; Mammetkuliev, M.; Shi, H.; Hou, B.; Bhattacharyya, D.; Zhao, B.; Cronin, S. B.; Benderskii, A. V. Asymmetric response of interfacial water to applied electric fields. *Nature* **2021**, *594* (7861), 62−65.

(21) Velasco-Velez, J.-J.; Wu, C. H.; Pascal, T. A.; Wan, L. F.; Guo, J.; Prendergast, D.; Salmeron, M. The structure of interfacial water on gold electrodes studied by x-ray absorption spectroscopy. *Science* **2014**, *346* (6211), 831−834.

(22) Wu, D. Y.; Li, J. F.; Ren, B.; Tian, Z. Q. Electrochemical surface-enhanced Raman spectroscopy of nanostructures. *Chem. Soc. Rev.* **2008**, *37* (5), 1025−1041.

(23) Nie, S.; Emory, S. R. Probing Single Molecules and Single Nanoparticles by Surface-Enhanced Raman Scattering. *Science* **1997**, *275* (5303), 1102−1106.

(24) Kneipp, K.; Wang, Y.; Kneipp, H.; Perelman, L. T.; Itzkan, I.; Dasari, R. R.; Feld, M. S. Single Molecule Detection Using Surface-Enhanced Raman Scattering (SERS). *Phys. Rev. Lett.* **1997**, *78* (9), 1667.

(25) Ma, Y.; Sikdar, D.; Fedosyuk, A.; Velleman, L.; Klemme, D. J.; Oh, S.-H.; Kucernak, A. R. J.; Kornyshev, A. A.; Edel, J. B. Electrotunable Nanoplasmonics for Amplified Surface Enhanced Raman Spectroscopy. *ACS Nano* **2020**, *14* (1), 328−336.

(26) Hill, R. T.; Mock, J. J.; Urzhumov, Y.; Sebba, D. S.; Oldenburg, S. J.; Chen, S.-Y.; Lazarides, A. A.; Chilkoti, A.; Smith, D. R. Leveraging Nanoscale Plasmonic Modes to Achieve Reproducible Enhancement of Light. *Nano Lett.* **2010**, *10* (10), 4150−4154.

(27) Sonnichsen, C.; Reinhard, B. M.; Liphardt, J.; Alivisatos, A. P. A molecular ruler based on plasmon coupling of single gold and silver nanoparticles. *Nat. Biotechnol.* **2005**, *23* (6), 741−745.

(28) Liu, N.; Hentschel, M.; Weiss, T.; Alivisatos, A. P.; Giessen, H. Three-Dimensional Plasmon Rulers. *Science* **2011**, *332* (6036), 1407−1410.

(29) Uphoff, S.; Holden, S. J.; Le Reste, L.; Periz, J.; van de Linde, S.; Heilemann, M.; Kapanidis, A. N. Monitoring multiple distances within a single molecule using switchable FRET. *Nat. Meth.* **2010**, *7* (10), 831−836.

(30) Herbert, J. M.; Coons, M. P. The Hydrated Electron. *Annu. Rev. Phys. Chem.* **2017**, *68* (1), 447−472.

(31) Tauber, M. J.; Mathies, R. A. Structure of the Aqueous Solvated Electron from Resonance Raman Spectroscopy: Lessons from Isotopic Mixtures. *J. Am. Chem. Soc.* **2003**, *125* (5), 1394−1402.
(32) Tauber, M. J.; Mathies, R. A. Resonance Raman spectra and vibronic analysis of the aqueous solvated electron. *Chem. Phys. Lett.* **2002**, *354* (5−6), 518−526.
(33) Tauber, M. J.; Stuart, C. M.; Mathies, R. A. Resonance Raman Spectra of Electrons Solvated in Liquid Alcohols. *J. Am. Chem. Soc.* **2004**, *126* (11), 3414−3415.
(34) Oudenhuijzen, M. K.; Bitter, J. H.; Koningsberger, D. C. The Nature of the Pt−H Bonding for Strongly and Weakly Bonded Hydrogen on Platinum. A XAFS Spectroscopy Study of the Pt−H Antibonding Shaperesonance and Pt−H EXAFS. *J. Phys. Chem. B* **2001**, *105* (20), 4616−4622.
(35) Borgschulte, A.; Gremaud, R.; Griessen, R. Interplay of diffusion and dissociation mechanisms during hydrogen absorption in metals. *Phys. Rev. B* **2008**, *78* (9), 094106.
(36) Langhammer, C.; Zhdanov, V. P.; Zorić, I.; Kasemo, B. Size-Dependent Kinetics of Hydriding and Dehydriding of Pd Nanoparticles. *Phys. Rev. Lett.* **2010**, *104* (13), 135502.
(37) Liu, Q.; Xu, W.; Huang, H.; Shou, H.; Low, J.; Dai, Y.; Gong, W.; Li, Y.; Duan, D.; Zhang, W.; et al. Spectroscopic visualization of reversible hydrogen spillover between palladium and metal−organic frameworks toward catalytic semihydrogenation. *Nat. Commun.* **2024**, *15* (1), 2562.
(38) Toscano, G.; Straubel, J.; Kwiatkowski, A.; Rockstuhl, C.; Evers, F.; Xu, H.; Asger Mortensen, N.; Wubs, M. Resonance shifts and spill-out effects in self-consistent hydrodynamic nanoplasmonics. *Nat. Commun.* **2015**, *6* (1), 7132.
(39) Yan, W. Hydrodynamic theory for quantum plasmonics: Linear-response dynamics of the inhomogeneous electron gas. *Phys. Rev. B* **2015**, *91* (11), 115416.
(40) Ciracì, C.; Della Sala, F. Quantum hydrodynamic theory for plasmonics: Impact of the electron density tail. *Phys. Rev. B* **2016**, *93* (20), 205405.
(41) Ding, K.; Chan, C. T. Plasmonic modes of polygonal rods calculated using a quantum hydrodynamics method. *Phys. Rev. B* **2017**, *96* (12), 125134.
(42) Bürgi, L.; Brune, H.; Kern, K. Imaging of Electron Potential Landscapes on Au(111). *Phys. Rev. Lett.* **2002**, *89* (17), 176801.
(43) Atkin, R.; Borisenko, N.; Drüschler, M.; El Abedin, S. Z.; Endres, F.; Hayes, R.; Huber, B.; Roling, B. An in situSTM/AFM and impedance spectroscopy study of the extremely pure 1-butyl-1-methylpyrrolidinium tris(pentafluoroethyl)trifluorophosphate/Au(111) interface: potential dependent solvation layers and the herringbone reconstruction. *Phys. Chem. Chem. Phys.* **2011**, *13* (15), 6849−6857.
(44) Li, C.-Y.; Le, J.-B.; Wang, Y.-H.; Chen, S.; Yang, Z.-L.; Li, J.-F.; Cheng, J.; Tian, Z.-Q. In situ probing electrified interfacial water structures at atomically flat surfaces. *Nat. Mater.* **2019**, *18* (7), 697−701.
(45) Li, C.-Y.; Duan, S.; Wen, B.-Y.; Li, S.-B.; Kathiresan, M.; Xie, L.-Q.; Chen, S.; Anema, J. R.; Mao, B.-W.; Luo, Y.; Tian, Z.-Q.; Li, J.-F. Observation of inhomogeneous plasmonic field distribution in a nanocavity. *Nat. Nanotechnol.* **2020**, *15* (11), 922−926.
(46) Andersen, J. E. T.; Kornyshev, A. A.; Kuznetsov, A. M.; Madsen, L. L.; Møller, P.; Ulstrup, J. Electron tunnelling in electrochemical processes and in situ scanning tunnel microscopy of structurally organized systems. *Electrochim. Acta* **1997**, *42* (5), 819−831.
(47) Frens, G. Controlled Nucleation for the Regulation of the Particle Size in Monodisperse Gold Suspensions. *Nat. Phys. Sci.* **1973**, *241*, 20−22.
(48) Jiang, Y.-X.; Li, J.-F.; Wu, D.-Y.; Yang, Z.-L.; Ren, B.; Hu, J.-W.; Chow, Y. L.; Tian, Z.-Q. Characterization of surface water on Au core Pt-group metal shell nanoparticles coated electrodes by surface-enhanced Raman spectroscopy. *Chem. Commun.* **2007**, *44*, 4608−4610.
(49) Tian, Z.-Q.; Ren, B.; Li, J.-F.; Yang, Z.-L. Expanding generality of surface-enhanced Raman spectroscopy with borrowing SERS activity strategy. *Chem. Commun.* **2007**, *34*, 3514−3534.
(50) Li, J.-F.; Yang, Z.-L.; Ren, B.; Liu, G.-K.; Fang, P.-P.; Jiang, Y.-X.; Wu, D.-Y.; Tian, Z.-Q. Surface-Enhanced Raman Spectroscopy Using Gold-Core Platinum-Shell Nanoparticle Film Electrodes: Toward a Versatile Vibrational Strategy for Electrochemical Interfaces. *Langmuir* **2006**, *22* (25), 10372−10379.
(51) Kresse, G.; Furthmüller, J. Efficient iterative schemes for ab initio total-energy calculations using a plane-wave basis set. *Phys. Rev. B* **1996**, *54* (16), 11169−11186.
(52) Kresse, G.; Joubert, D. From ultrasoft pseudopotentials to the projector augmented-wave method. *Phys. Rev. B* **1999**, *59* (3), 1758−1775.
(53) Perdew, J. P.; Burke, K.; Ernzerhof, M. Generalized Gradient Approximation Made Simple. *Phys. Rev. Lett.* **1996**, *77* (18), 3865−3868.
(54) Methfessel, M.; Paxton, A. T. High-precision sampling for Brillouin-zone integration in metals. *Phys. Rev. B* **1989**, *40* (6), 3616−3621.
(55) Kolb, M. J.; Calle-Vallejo, F.; Juurlink, L. B. F.; Koper, M. T. M. Density functional theory study of adsorption of H2O, H, O, and OH on stepped platinum surfaces. *J. Chem. Phys.* **2014**, *140* (13), 134708.
(56) Duan, S.; Tian, G.; Ji, Y.; Shao, J.; Dong, Z.; Luo, Y. Theoretical Modeling of Plasmon-Enhanced Raman Images of a Single Molecule with Subnanometer Resolution. *J. Am. Chem. Soc.* **2015**, *137* (30), 9515−9518.

https://doi.org/10.1021/jacs.5c09908
J. Am. Chem. Soc. 2025, 147, 29468−29477